Wake characteristics of pumping mode airborne wind energy systems

IOP Conf. Series: Journal of Physics: Conf. Series **1256** (2019) 012016 doi:10.1088/1742-6596/1256/1/012016

Wake characteristics of pumping mode airborne wind energy systems

T. Haas[1], J. De Schutter[2], M. Diehl[2,3] and J. Meyers[1]

[1]KU Leuven, Department of Mechanical Engineering, Celestijnenlaan 300, BE-3001 Leuven, Belgium,
[2]University of Freiburg, Department of Microsystems Engineering, Georges-Köhler-Allee 102, DE-79110 Freiburg, Germany,
[3]University of Freiburg, Department of Mathematics, Georges-Köhler-Allee 102, DE-79110 Freiburg, Germany

E-mail: thomas.haas@kuleuven.be

Abstract. Airborne wind energy is an emerging technology that aims at harvesting wind power at high altitudes. In the present work, we propose a framework combining optimal control and large-eddy simulation to investigate the wake characteristics of large-scale airborne wind energy systems. We consider systems operating in pumping mode which alternate between power-generating and -consuming phases. We investigate the downstream wake development in non-turbulent and turbulent sheared inflow conditions. The optimal system operation leads to a non-uniform radial wake development and results show that the maximal wake velocity deficit for the current system is half the deficit predicted by Betz limit for a conventional wind turbine.

1. Introduction

Harvesting wind power using tethered aircraft was presented for the first time by Loyd back in 1980 [1] when he introduced different concepts for power generation. One of them is the pumping mode, which is the object of this study. Pumping-mode airborne wind energy systems (AWES) operate in alternating power-generating and power-consuming phases. In the first phase, the tethered airborne device flies crosswind maneuvers that generate a high lift force, which is in turn transferred to the ground in form of tether tension. This tension is then used to unwind the tether from a winch. A generator connected to the winch transforms its rotation into electrical power. In the second phase, the airborne device is recovered by simultaneously controlling its flight path towards its original location and reeling in the tether. This periodic flight trajectory is optimized in such a way that the power required for the recovery phase is only a fraction of the power harvested during generation phase.

In his work, Loyd gave as an example, an aircraft with a wingspan of 68 meters generating approximately 7 MW of power. As of today, prototypes with wingspans ranging from 5 to 25 meters were developed, generating up to several hundred kilowatts of power. Leading companies have unveiled their plans to develop utility-scale devices in the multi-megawatts range [2][3], with dimensions similar to the example given by Loyd. For an overview of the implemented concepts, please refer to the aforementioned references.

In order to precisely estimate the AWES behavior, accurate modeling of its dynamics is required. Different models and control strategies are presented in [4] and [5]. Optimization

of the flight trajectory in order to increase the system performance is discussed in [6]. Model validation by means of system identification is given in [7].

Understanding the interaction between AWES and the wind flow is fundamental for accurate performance prediction but also for flight stability and farm operation. Flow-system interaction was neglected in the modeling procedure outlined in [5] but recent studies, considering flow induction based on blade-element/momentum theory, reported significant decrease in power extraction [8][9]. For conventional wind turbines, flow interaction and its effects on wake patterns and power extraction have been thoroughly investigated using numerical simulations [10][11]. In previous work [12], wake characteristics of on-board generation AWES were assessed by means of large-eddy simulations (LES). In this study, we focus on the analysis of pumping-mode AWES.

This paper is organized as follows. In Section 2, we introduce the modeling strategies employed to describe the airborne wind energy system and compute its flight path. The large-eddy simulation framework and the coupling with the system's dynamics are introduced in Section 3. In Section 4, the results of numerical simulations are presented and discussed. An outlook concludes this paper and also provides motivation for future work in Section 5.

2. modeling of airborne wind energy systems

2.1. Utility-scale AWES

The AWES design used in the following is derived from a semi-empirical study based on available manufacturer data from [2][3] and simple scaling laws of aerodynamics. The aim of the design study is to specify a set of qualitative parameters for the choice of initial wing and tether dimensions. The final tether dimensions are optimized along with the flight trajectory. In this study, we consider a wingspan $b = 60.0\,\mathrm{m}$ as the driving design parameter.

The wing mass is fitted using data from the manufacturer Makani Power [3] using a power law $f(b) = c_0 \cdot b^{c_1}$ with constant coefficients $c_0 \approx 0.148$ and $c_1 \approx 2.7$. The wing mass scales with the wingspan to a power coefficient $2.0 < c_1 < 3.0$, which is consistent with the scaling of wing volume. However, Makani's devices carry additional weight from on-board turbines, thus the mass of the wing is slightly overestimated for a pumping-mode AWES. The expected rated power of the system is also fitted from available manufacturer data using a similar power law with $c_0 \approx 3943$ and $c_1 \approx 1.72$. The maximal power that an AWES can extract from the wind is given in [13] and reads

$$P = \frac{4}{27}\left(\frac{1}{2}\rho V_{\mathrm{w}}^3\right)\frac{b^2}{AR}\left(\frac{C_{\mathrm{L}}^3}{C_{\mathrm{D}}^2}\right), \tag{1}$$

where ρ is the air density. Hence, we can derive the requirements on the wing lift and system drag coefficients C_{L} and C_{D}, and on the wing aspect ratio AR such that expected power output and maximal power match for a given rated wind speed of $V_{\mathrm{w}} = 9.0\,\mathrm{m/s}$[3].

The design process consists in defining wing and tether dimensions for a set of different airfoils in order to find appropriate values of C_{L}, C_{D} and AR, such that the system performance complies with the expected power at the given wingspan. We assume standard reference conditions for air at a temperature $T = 15.0\,^{\circ}\mathrm{C}$ and pressure $p = 1.0\,\mathrm{atm}$. Using the open-source software XFLR5 (*www.xflr5.com*), we compute the airfoil's lift and drag polars $c_{\mathrm{l}}(\alpha)$ and $c_{\mathrm{d}}(\alpha)$ at a chord-based Reynolds number $Re_{\mathrm{c}} = 10^7$, with α the angle-of-attack. For a specific range of angles-of-attack, the lift distribution is linear and can be expressed as $c_{\mathrm{l}}(\alpha) = a_0\,(\alpha - \alpha_{\mathrm{L=0}})$ by thin-airfoil theory[14], with $a_0 = 2\pi$ the lift slope and $\alpha_{\mathrm{L=0}}$ the zero-lift angle-of-attack extrapolated from the lift polar. This theory can be extended to finite wings with elliptical wing planform and no twist, such that lift and drag coefficients of the wing read

$$C_{\mathrm{L}} = \frac{a_0}{1 + \frac{a_0}{\pi AR}}\left(\alpha - \alpha_{\mathrm{L=0}}\right), \qquad C_{\mathrm{D,W}} = c_{\mathrm{d}}(\alpha) + \frac{C_{\mathrm{L}}^2}{\pi AR}. \tag{2}$$

Table 1. Wing characteristics and initial tether dimensions

Quantity	b	S	AR	m_W	d_T	L_T	$C_\mathrm{D,T}$	ρ_T	m_T
Units	m	m^2	–	kg	mm	m	–	$\mathrm{kg/m}^3$	kg
AWES	60	138.5	26	8000	27.7	1000	0.0501	970.0	586.8

While final tether dimensions are optimized at a later stage, initial estimates of tether length L_T and diameter d_T are required to compute the tether drag coefficient. The maximal tether length is set to $L_\mathrm{T} = 1000.0\,\mathrm{m}$, comparable to the value specified in [3]. The diameter is chosen such that it withstands a high tension similar to the lift force generated by the wing, as given in [15]. The lift force is computed for an apparent wind speed $V_\mathrm{a} = (2/3)(C_\mathrm{L}/C_\mathrm{D})V_\mathrm{w}$, using the values $C_\mathrm{L} = 1.0$ and $C_\mathrm{D} = 0.07$ suggested in [13]. Finally, assuming the drag coefficient of a cylinder at high Reynolds number $C_\mathrm{D,cyl} = 1.0$, the tether drag coefficient reads

$$C_\mathrm{D,T} = \frac{1}{4}\frac{d_\mathrm{T} \cdot L_\mathrm{T}}{b^2/AR} C_\mathrm{D,cyl}. \tag{3}$$

For different airfoils, we compute the lift and total drag coefficients of the system, C_L and C_D, using airfoil polars and equations (2),(3), for a range of aspect ratios. We consider the critical angle-of-attack of the wing as operation point, however reduced by a safety margin of 3 degrees to take into account angle-of-attack variations caused by turbulence. At that point, we compute for each aspect ratio the power of the system according to equation (1) and compare it to the expected power from the power law fitted with manufacturer data. At large aspect ratios, wing surface and induced wing drag are decreased, thus we opt for the airfoil with the largest aspect ratio, the SD7032 airfoil. This airfoil is also used by the company TwingTec in [16]. The dimensions of the system, also including wing area S, tether material density ρ_T and wing and tether masses m_W and $m_\mathrm{T} = \rho_\mathrm{T}(\pi d_\mathrm{T}^2/4)L_\mathrm{T}$, are summarized in Table 1.

2.2. modeling of AWES dynamics

The aim of our modeling effort is to capture the main dynamic effects of a tethered wing, while obtaining system dynamics that are computationally tractable and tailored for optimal control purposes. A well-established modeling procedure for AWES is based on representations in non-minimal coordinates and derivation of the model equations with Lagrangian mechanics [4] and is adopted in this paper. In this study a simplified point-mass model is used, as proposed in [5].

The proposed Lagrangian-based modeling procedure applied to a tethered point-mass results in an implicit index-1 differential algebraic equation (DAE) representation summarized by

$$F(\dot{x}(t), x(t), u(t), z(t), \theta, p) = 0, \tag{4}$$

with associated consistency conditions. Here, the state vector $x = (q, \dot{q}, C_\mathrm{L}, \psi, l, \dot{l}, \ddot{l})^\top$ comprises of firstly the wing position q and velocity $\dot{q}$. The instantaneous lift coefficient C_L and roll angle ψ are assumed to be directly controlled. Finally, the variables l, $\dot{l}$ and $\ddot{l}$ represent tether length, speed and acceleration respectively. The control vector $u = (\dot{C}_\mathrm{L}, \dot{\psi}, \dddot{l})^\top$ consists of the derivatives of lift coefficient and roll angle, and the tether jerk. The algebraic variable $z = \lambda$ is the Lagrange multiplier related to the constraint $c(q) = \frac{1}{2}\left(q^T q - l^2\right)$, which forces the wing's translational dynamics to evolve on a 2D manifold defined by the tether direction and length. The variable θ are system parameters that can be optimized, in this case the tether

Table 2. Variable bounds used in optimal control problem (9)

ν	$\nu_{\min}$	$\nu_{\max}$	units	ν	$\nu_{\min}$	$\nu_{\max}$	units
C_{L}	$C_{\mathrm{L}}\big\vert_{\alpha_{\min}}$	$C_{\mathrm{L}}\big\vert_{\alpha_{\max}}$	-	λ	0	∞	N/m
$\dot{C}_{\mathrm{L}}$	-5	5	1/s	q_{z}	$2b$	∞	m
ψ	-80	+80	deg	$\ddot{l}$	-10	+10	$\mathrm{m/s^2}$
$\dot{\psi}$	-285	+285	deg/s	$\dddot{l}$	-100	+100	$\mathrm{m/s^3}$

diameter d_{T}. Finally, the use of constant parameters $p = (m_{\mathrm{W}}, b, S, AR, u_*, z_0)^\top$ allow the system dynamics to be evaluated for different wing sizes and wind profiles. Here, additional to the wing geometry, relevant parameters are the friction velocity u_* and surface roughness z_0 that define the logarithmic wind profile given by $U(q_{\mathrm{z}}) = u_*/\kappa \ln(q_{\mathrm{z}}/z_0)$. Following the procedure outlined in [4], the equations of motion can be shown to read

$$\begin{bmatrix} \left(m_{\mathrm{W}} + \frac{1}{2}m_{\mathrm{T}}\right) I & q \\ q^\top & 0 \end{bmatrix} \begin{bmatrix} \ddot{q} \\ \lambda \end{bmatrix} = \begin{bmatrix} F_q - \left(m_{\mathrm{W}} + \frac{1}{2}m_{\mathrm{T}}\right) g \mathbb{1}_{\mathrm{z}} \\ -\dot{q}^\top \dot{q} + \dot{l}^2 + l\ddot{l} \end{bmatrix} \tag{5}$$

The external forces acting on the system are $F_{\mathrm{q}} = F_{\mathrm{L}} + F_{\mathrm{D}}$, with F_{L} the aerodynamic lift force, and F_{D} the combined drag force of wing and tether. According to [17], we define the reference frame of the AWES $R = [e_1, e_2, e_3]^\top$. The roll axis e_1 is assumed to be always aligned with the apparent wind speed, defined as $V_{\mathrm{a}} = V_{\mathrm{w}} - \dot{q}$ with the wind vector $V_{\mathrm{w}} = [U(q_{\mathrm{z}}), 0, 0]$. The transversal axis e_2 is orthogonal to the plane formed by the vectors e_1 and $e_{\mathrm{r}} = q/||q||$. The frame is completed with the third axis $e_3 = e_1 \times e_2$, pointing up. The density variation with height is modeled with international standard atmosphere model, using the parameters found in [5]. The aerodynamic forces acting on the system read

$$F_{\mathrm{L}} = \frac{1}{2}\rho(q_{\mathrm{z}}) S C_{\mathrm{L}} ||V_{\mathrm{a}}||^2 \left(\cos(\psi) e_3 - \sin(\psi) e_2\right), \tag{6}$$

$$F_{\mathrm{D}} = \frac{1}{2}\rho(q_{\mathrm{z}}) S (C_{\mathrm{D,W}} + C_{\mathrm{D,T}}) ||V_{\mathrm{a}}||^2 e_1. \tag{7}$$

Together with (5), the following trivial kinematics complete the implicit DAE (4)

$$\frac{\mathrm{d}}{\mathrm{d}t}(q, C_{\mathrm{L}}, \psi, l, \dot{l}, \ddot{l})^\top = (\dot{q}, \dot{C}_{\mathrm{L}}, \dot{\psi}, \dot{l}, \ddot{l}, \dddot{l})^\top. \tag{8}$$

2.3. Optimal control of AWES

The dynamics presented in the previous section can be used to generate periodic flight trajectories with optimal control techniques. During operation, the AWES has to satisfy a set of constraints $h(\dot{x}(t), x(t), u(t), z(t), \theta, p) \leq 0$. These constraints limit the wing acceleration to a hardware-friendly range and ensure that maximum tether stress is not exceeded (We consider a safety factor $f_{\mathrm{s}} = 3$ and a tether yield strength $\sigma_{\max} = 3.09\,\mathrm{GPa}$). Additional constraints represent variable bounds that ensure validity of the aerodynamic model (operation within linear region) and the tether model (positive tether force), as well as to limit mechanical stress on the tether winch. Table 2 summarizes the variable bounds. Note that the kite's center of mass is restricted to fly at a minimal distance of two wingspans above the ground.

Given the dynamics (4) and constraints h, the periodic optimal control problem (OCP) reads:

$$\min_{x(t),u(t),z(t),\theta,T} \quad -\frac{1}{T}\int_0^T \lambda(t) l(t) \dot{l}(t) dt \tag{9a}$$

$$\text{s.t.} \quad F(\dot{x}(t), x(t), u(t), z(t), \theta, p) = 0, \tag{9b}$$

$$h(\dot{x}(t), x(t), u(t), z(t), \theta, p) \leq 0, \tag{9c}$$

$$x(0) - x(T) = 0 \tag{9d}$$

The cost function is defined as the average mechanical power output of the system and T is the time period of the cycle. The OCP is parametric in p and can thus be solved for different designs and wind profiles. Initial and terminal state can be chosen freely, but must be equal.

The OCP is implemented and solved with the open-source AWE optimization framework `awebox` [18]. The problem is discretized with $N = 80$ intervals, using the direct collocation approach based on a Radau scheme with polynomial order 4. Within `awebox`, the resulting nonlinear program is formulated using the symbolic framework CasADi [19] and solved with the interior-point solver IPOPT [20] using the linear solver MA57 [21].

3. Large-eddy simulation framework

3.1. Governing equations of LES

The interaction between AWES and wind resource is computed by means of large-eddy simulations (LES). The simulations are performed using the code SP-Wind developed in-house at KU Leuven [11]. The governing equations are the filtered incompressible Navier-Stokes equations for neutral flows. The continuity and momentum equations read

$$\partial_i \tilde{u}_i = 0\,, \tag{10}$$

$$\partial_t \tilde{u}_i + \partial_j\left(\tilde{u}_i \tilde{u}_j\right) = -\partial_i \tilde{p}^* - \partial_j \tau_{ij}^d - \delta_{i1}\partial_1 p_\infty/\rho + \bar{F}_i \tag{11}$$

where the filtered velocity is denoted by $\tilde{u}_i$. τ_{ij} is the subgrid-scale stress tensor. Its deviatoric part τ_{ij}^d is modelled using an eddy-viscosity model and its trace is included in the filtered modified pressure given by $\tilde{p}^* = \tilde{p}/\rho + \tau_{kk}/3 - p_\infty/\rho$. The flow is driven by a constant imposed pressure gradient $\partial_1 p_\infty/\rho$ which sets the value of the friction velocity u_* in the logarithmic inflow profile. The effects of the AWES on the flow are modeled as body force $\bar{\boldsymbol{F}}$ and are derived below.

The governing equations are discretized as follows: in the horizontal directions (x_1, x_2), a Fourier pseudo-spectral method is used. This discretization method requires periodic boundary conditions which can be circumvented in the streamwise direction x_1 by employing a fringe-region technique. In the vertical direction (x_3), a fourth-order energy-conserving finite-difference scheme is used. A classic four-stage fourth-order Runge Kutta scheme is applied to perform time integration. For more details on the implementation of SP-Wind, please refer to [22]. Finally, turbulence based on the Mann model [23] is generated using the *tugen* library [24] and is superimposed on the logarithmic inflow profile in the fringe region.

3.2. Actuator sector method

In the current work, we do not compute the flow around the AWES by means of mesh-resolved simulations, but instead, we model the effects of the AWES on the flow by adding a forcing term $\bar{F}_i$ to the momentum equations. We do so by using a similar method to the actuator sector method (ASM) introduced by [25]. The ASM stems from a family of methods such as the actuator disk and actuator line methods, that have proven their abilities to reproduce wake characteristics of conventional wind turbines with a good degree of accuracy [26].

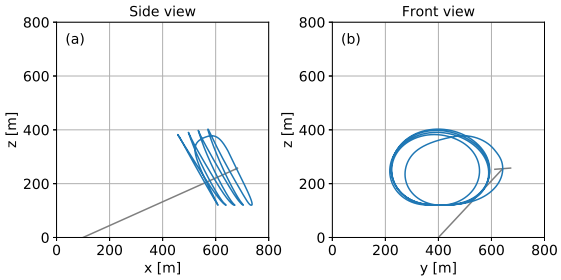

Figure 1. Optimal AWES trajectory.

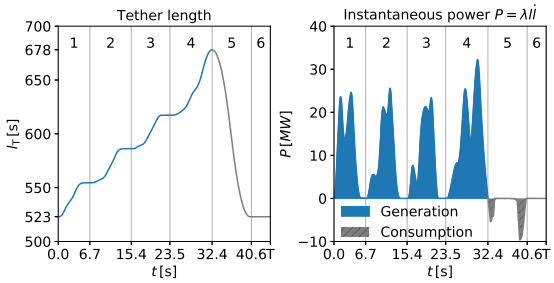

Figure 2. Tether length and AWES power.

The system components are discretized into a finite number of segments for which the local aerodynamic forces are computed and subsequently smoothed out onto the LES grid. In the present study, the tether is not discretized separately. As the tether drag scales linearly with the tether length and with the square of the apparent wind speed, its effect on the flow prevails in the direct vicinity of the wing. Based on that assumption, we add the complete tether drag force close to the attachment point on the wing.

We assume that the dynamics of the system are not sensitive to the small variations in apparent wind velocity induced by the turbulent flow. Given the fact that the crosswind AWES speed is approximately 12 times higher than the wind speed, this is a reasonable approximation. Thus, the position of the system, its speed and its orientation can directly be taken from the optimization results. For each segment of the wing, we interpolate the local wind speed from the LES grid to its central position and compute the apparent wind velocity. Given the orientation of the wing, we can calculate the local angle of attack and derive the lift and drag coefficients from the airfoil polars. To achieve the aerodynamic behavior assumed in the dynamic model, the wing planform requires to follow an elliptical distribution, thus the chord length of each segment is computed accordingly. For each segment k, we eventually compute the force per unit segment length $\boldsymbol{F}_\mathrm{k}(\tilde{u}, q)$.

The aerodynamic forces of each segment are then spread out over the closest LES grid cells of the simulation domain using a Gaussian convolution filter,

$$\hat{\boldsymbol{F}}(\boldsymbol{x}) = \int_{-b/2}^{b/2} \boldsymbol{F}_\mathrm{k}(\tilde{u}, r) G(||\boldsymbol{x} - r\boldsymbol{e}_2||) dr. \tag{12}$$

These forces are computed at each substep m of the AWES dynamics, which are much faster than the flow dynamics. Thus, in an additional step, the spatially distributed forces $\hat{\boldsymbol{F}}$ computed within a time step of the LES simulation are filtered in time using an exponential filter,

$$\bar{\boldsymbol{F}}^m = (1-\gamma)\bar{\boldsymbol{F}}^{m-1} + \gamma\hat{\boldsymbol{F}}^m, \tag{13}$$

where the filter constant $\gamma = \delta t/(0.75\Delta t + \delta t)$ with δt and Δt the timesteps of the AWES dynamics and LES simulation, respectively. These body forces, being time and spatially filtered, are subsequently added to the momentum equation as the source term $\bar{\boldsymbol{F}}$.

4. Characteristics of pumping-mode AWES

4.1. Dynamics of AWES

We present here the OCP results. These results were generated assuming a logarithmic velocity distribution given a friction velocity $u_* \approx 0.3048\,\mathrm{m/s}$ and a roughness length $z_0 = 0.0002\,\mathrm{m}$, where the axial velocity component is aligned with the x-direction. Thus, in the following, the (x, y, z)-coordinates represent the stream-wise, cross-wind and vertical directions respectively.

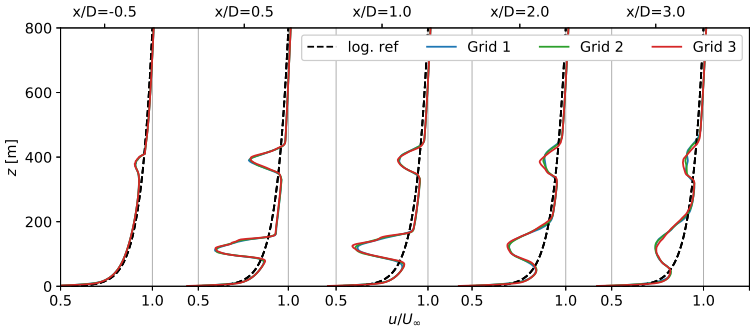

Figure 3. Time-averaged vertical profiles of axial velocity component at several downstream locations given a sheared inflow without turbulence computed on grid 2.

The periodic trajectory flown by the AWES is shown in Figure 1, where the trajectory is projected onto the (xz)-plane (a) and the (yz)-plane (b). The periodic trajectory consists of four consecutive power-generating phases (1-4) followed by a retraction phase (5) and a final transition phase (6), as shown in Figure 2. In the generation phases, the system flies upward against the wind at a fixed tether length, whereas the tether is reeled-out when the system flies downward with the wind. The system is recovered during the retraction phase lowering the generated lift such that the tether can be reeled-in at lower tether tension. Given the aforementioned offshore wind conditions, the average power generated by the AWES is approximately 7.5 MW.

4.2. Computation setup and grid analysis

As mentioned in Section 3, the flow domain is discretized into a finite number of grid cells. The domain dimensions are chosen such that the blockage ratio of the projected area flown by the system does not exceed 10% of the inflow section area, and the length of the domain allows for 1800 m of downwind wake development. In order to reproduce accurately the effect of the AWES onto the flow, the size of the cells is chosen such that the wing of the system spans over several grid locations. A grid refinement study was performed using three different grids, for which the wingspan spans over approximately 7, 10 and 15 grid cells respectively. The ratio of the width of the Gaussian force filter h to the grid size was kept constant, $h/\Delta_x = 1.5$, where Δ_x is the size of a stream-wise cell. The specifications of the different grids are given in Table 3.

In the following, all locations are specified relative to the central point of the trajectory defined as $(x_0, y_0, z_0) = (600.0\,\text{m}, 400.0\,\text{m}, 260.0\,\text{m})$, with $D = 280\,\text{m}$ the difference between highest and lowest altitudes flown by the AWES. Figure 3 shows time-averaged vertical profiles of the axial velocity component for a sheared inflow without addition of turbulence. The profiles of the three grids overlap for both the near wake $(x/D = 0.5)$ and the far wake $(x/D = 3.0)$. Thereafter, simulations using low-resolution grids are sufficient to capture the main patterns of the wake. However we prefer to use higher resolutions to capture more detailed flow features.

For turbulence generation using the Mann model, we choose the turbulent length scale $L = 33.6\,\text{m}$, the degree of anisotropy $\Gamma = 3.9$ and the Kolmogorov constant α and viscous dissipation rate of turbulent kinetic energy ϵ such that $\alpha\epsilon^{2/3} = 0.3\,\text{m}^{4/3}\text{s}^{-2}$, according to [22].

The aerodynamic forces acting onto the system over one periodic cycle are shown in Figure 4. We show the components of the total sector forces applied onto the domain for the simulations with non-turbulent and turbulent inflows and compare them to the reference from the OCP. During the retraction phase, the forces on the system dramatically drop in stream-wise and vertical directions. Also, sector forces for both inflow conditions reproduce with acceptable

Table 3. Domain size and grid resolution for the grid analysis

Grid 1	Domain size	$L_x \times L_y \times L_z$	=	$2720.0\,\text{m} \times 800.0\,\text{m} \times 800.0\,\text{m}$
	Grid resolution	$\Delta_x \times \Delta_y \times \Delta_z$	=	$8.0\,\text{m} \times 8.0\,\text{m} \times 4.0\,\text{m}$
	Grid size	$N_x \times N_y \times N_z$	=	$340 \times 100 \times 200$
Grid 2	Domain size	$L_x \times L_y \times L_z$	=	$2700.0\,\text{m} \times 800.0\,\text{m} \times 800.0\,\text{m}$
	Grid resolution	$\Delta_x \times \Delta_y \times \Delta_z$	=	$6.25\,\text{m} \times 6.25\,\text{m} \times 3.125\,\text{m}$
	Grid size	$N_x \times N_y \times N_z$	=	$432 \times 128 \times 256$
Grid 3	Domain size	$L_x \times L_y \times L_z$	=	$2720.0\,\text{m} \times 800.0\,\text{m} \times 800.0\,\text{m}$
	Grid resolution	$\Delta_x \times \Delta_y \times \Delta_z$	=	$4.0\,\text{m} \times 4.0\,\text{m} \times 2.0\,\text{m}$
	Grid size	$N_x \times N_y \times N_z$	=	$680 \times 200 \times 400$

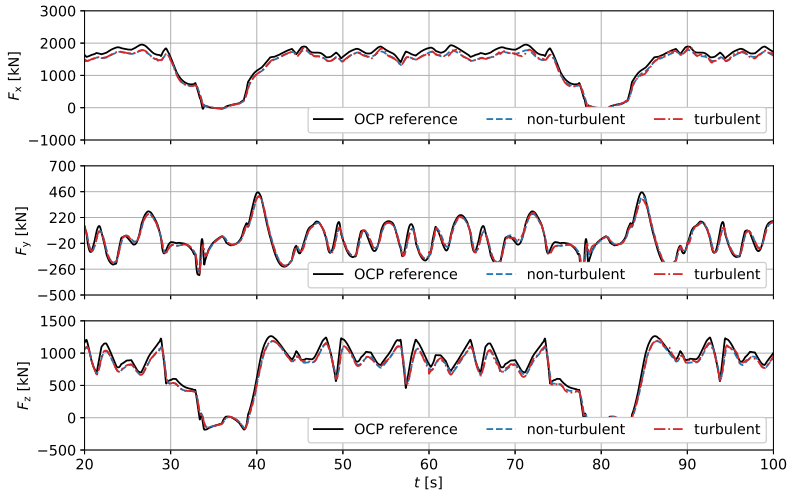

Figure 4. Components of the reference and sector forces for non-turbulent and turbulent inflows computed on grid 2.

accuracy the reference forces given the time lag from the exponential time filtering. This is due to the fact that fluctuations in local wind speed do not affect much the apparent wind seen by the system, since its main component, the crosswind flight speed, is approximately 12 times higher than the wind speed. The unsteadiness and periodicity of the force distribution will however have an influence on the downstream development of the wake, as shown in the following section.

4.3. LES results

The specificities of the AWES trajectory and the unsteadiness of its loading are reflected into the dynamics of the wake development. Figure 5 shows the instantaneous field of the axial velocity component in vertical and horizontal planes for non-turbulent inflow using grid 3. Alternating patterns of generation and retraction phases are clearly seen in the AWES wake. During the four power-generating loops, the axial flow is slowed down by the strong loading from the wing and is then subject to turbulent mixing approximately 3D downstream. During recovery, the system almost exerts no force on the flow which advects downstream without much perturbation.

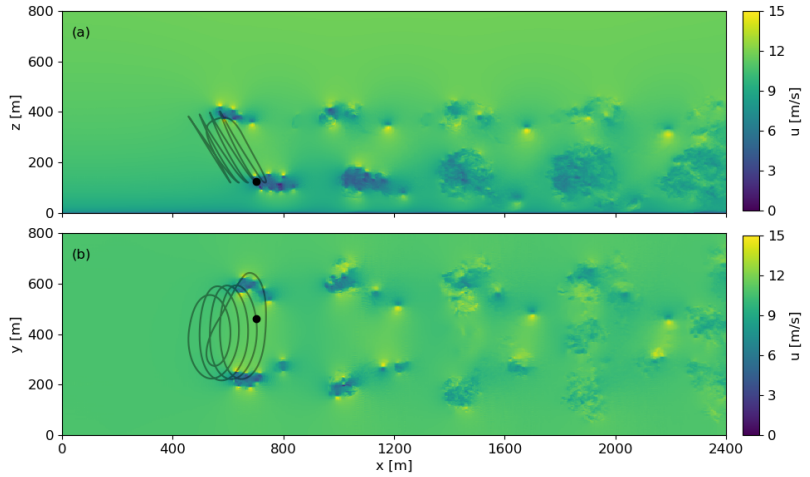

Figure 5. Instantaneous downstream flow development at $t = 200.0\,\mathrm{s}$. Axial velocity contours in the (a) (xz)-plane at $y = y_0$, and (b) (xy)-plane at $z = z_0$ computed for non-turbulent inflow conditions on grid 3. The dot indicates the position of the AWES.

Time-averaged flow fields deliver more insights on the wake characteristics. Velocity fields were averaged over a period $T = 3000\,\mathrm{s}$ with samples taken every second. This averaging period corresponds to approximately 67 periodic cycles of the AWES and 12 domain flow-through periods respectively. Figure 6 shows averaged profiles of the axial velocity component at several downstream locations computed for both non-turbulent (NT) and turbulent (TU) inflow conditions using grid 2. To ease the comparison between turbulent and non-turbulent case, the deviation $\Delta\bar{u}$ of the time-averaged turbulent velocity field (without AWES) $\bar{u}_\mathrm{t}$ from the reference logarithmic profile was subtracted from the profiles. Part (a) shows the velocity distribution over height taken in the middle of the domain at $y = y_0$ and highlights the difference between the profiles and the reference logarithmic velocity distribution. Part (b) shows spanwise profiles at two different heights $z = z_0 - D/2$ and $z = z_0 + D/2$.

These profiles show the height dependency of the radial wake development. These effects can be expected given the unsteady loading along the trajectory and the fact that the AWES flies on an tilted orbit, in comparison to the vertical rotation planes of conventional wind turbines. In the bottom part of the wake, at $z = z_0 - D/2$, the velocity deficit is stronger and the radial spreading of the wake more pronounced. In contrast, the top part of the wake at $z = z_0 + D/2$ recovers faster. As of the effects of turbulence on the wake development, we observe a less pronounced velocity deficit and a faster recovery induced by turbulent mixing.

We also consider axial flow induction of the AWES. We define an axial interference factor a given as $a = 1 - u(z)/U_\infty(z)$, with $u(z)$ the axial flow velocity and $U_\infty(z)$ the reference velocity from the logarithmic velocity profile at a specific height. This factor is a way to measure the impact of the system on the surrounding flow. A negative value indicates the speed-up of the flow, while a positive value indicates deceleration of the flow. For the turbulent inflow using Mann turbulence, the vertical profiles of time-averaged axial velocity do not converge to a logarithmic profile, thus we compute the interference factor a using the time-averaged turbulent velocity field $\bar{u}_\mathrm{t}(z)$ from LES without AWES as normalization value instead of $U_\infty(z)$. Figure 7 shows the local distribution of the induction factor in vertical planes computed on grid 2. The figure first confirms the flow acceleration inside and around the wake as well as the asymmetry of the wake shape. Again, no significant difference is observed between the non-turbulent and turbulent inflow case. In the central (yz)-plane of the trajectory, at $x = x_0$, values of a in

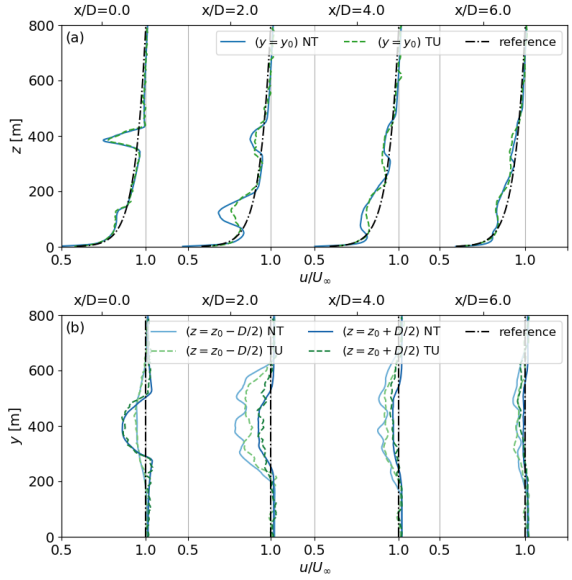

Figure 6. Time-averaged axial velocity distribution at several downstream locations. (a) Vertical and (b) horizontal profiles.

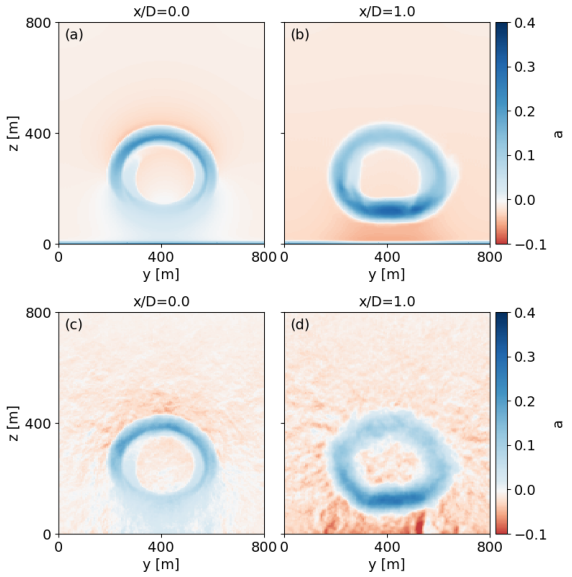

Figure 7. Distribution of axial induction factor at several downstream locations. (a-b) Non-turbulent and (c-d) turbulent inflow.

the range -0.04 to 0.22 are observed, which are mainly the wake effects of the four upstream power-generating loops. However, at $z = z_0 - D/2$, the induction factor is $a \approx 0.08$. This value, observed upstream of the trajectory, confirms that induction, even if limited, can not be neglected. Downstream of the trajectory, at $x = x_0 + D$, values in the range -0.05 to 0.31 are observed. The highest axial induction value recorded in the wake is $a = 0.335$. For conventional wind turbines, momentum theory predicts that one half of the velocity decrease occurs upstream of the rotor disk and another half occurs in the wake [27]. For maximal energy extraction, the Betz-Joukowsky limit defines an optimal value $a = 1/3$ corresponding to a maximal velocity decrease of $2/3$ in the wake. Therefore, the current results suggest that the velocity deficit in the wake of an AWES system is half the deficit of a conventional wind turbine.

5. Outlook

In the present study we have presented a simulation framework combining optimal control and large-eddy simulations in order to investigate the wake development of airborne wind energy systems operating in pumping mode. We first proposed a generic design of a large-scale AWES and presented its dynamics. The simulation results show the non-uniform radial wake development downstream of the trajectory flown by the system. The velocity decrease observed in the wake is half the velocity deficit predicted by the Betz limit for conventional wind turbines. This study motivates further work on wake interaction in the context of AWES farms in order to investigate the impact of wakes, first on the dynamics, and second on the power extraction of downstream systems.

Acknowledgments

This project has received funding from the European Union's Horizon 2020 research and innovation programme under the Marie Skłodowska-Curie grant agreement No 642682. The computational resources and services used in this work were provided by the VSC (Flemish Supercomputer Center), funded by the Research Foundation Flanders (FWO) and the Flemish

Government - department EWI.

References

[1] M L Loyd. Crosswind Kite Power. *Journal of Energy*, 4(3):106–111, 1980.
[2] M Kruijff and R Ruiterkamp. A roadmap towards airborne wind energy in the utility sector. In R Schmehl, editor, *Airborne Wind Energy: Advances in Technology Development and Research*, pages 643–662. Springer Singapore, 2018.
[3] Makani Power Inc. Response to the federal aviation authority. Technical report, 2017.
[4] S Gros and M Diehl. Modeling of airborne wind energy systems in natural coordinates. In Uwe Ahrens, Moritz Diehl, and Roland Schmehl, editors, *Airborne Wind Energy*, pages 181–203. Springer-Verlag Berlin Heidelberg, 2013.
[5] M Zanon, S Gros, and M Diehl. Model predictive control of rigid-airfoil airborne wind energy systems. In U Ahrens, M Diehl, and R Schmehl, editors, *Airborne Wind Energy*, pages 219–234. Springer-Verlag Berlin Heidelberg, 2013.
[6] G Horn, S Gros, and M Diehl. Numerical trajectory optimization for airborne wind energy systems described by high fidelity aircraft models. In U Ahrens, M Diehl, and R Schmehl, editors, *Airborne Wind Energy*, pages 205–218. Springer-Verlag Berlin Heidelberg, 2013.
[7] G Licitra, A Bürger, P Williams, R Ruiterkamp, and M Diehl. System identification of a rigid wing airborne wind energy system. 2017.
[8] M Zanon, S Gros, J Meyers, and M Diehl. Airborne wind energy: Airfoil-airmass interaction. pages 5814–5819, 2014.
[9] R Leuthold, S Gros, and M Diehl. Induction in optimal control of multiple-kite airborne wind energy systems. In *Proceedings of 20th IFAC World Congress, Toulouse, France*, 2017.
[10] Y T Wu and F Porté-Agel. Large-eddy simulation of wind-turbine wakes: Evaluation of turbine parametrisations. *Boundary-Layer Meteorology*, 138(3):345–366, 2011.
[11] M Calaf, C Meneveau, and J Meyers. Large eddy simulation study of fully developed wind-turbine array boundary layers. *Physics of Fluids*, 22(1):1–16, 2010.
[12] T Haas and J Meyers. Comparison study between wind turbine and power kite wakes. *Journal of Physics: Conference Series*, 854:012019, may 2017.
[13] M Diehl. Airborne wind energy: Basic concepts and physical foundations. In Uwe Ahrens, Moritz Diehl, and Roland Schmehl, editors, *Airborne Wind Energy*, pages 3–22. Springer-Verlag Berlin Heidelberg, 2013.
[14] J D Anderson. *Fundamentals of Aerodynamics*. McGraw-Hill, 2010.
[15] F Bauer, R M Kennel, C M Hackl, F Campagnolo, M Patt, and R Schmehl. Drag power kite with very high lift coefficient. *Renewable Energy*, 118:290–305, 2018.
[16] F Gohl and R H Luchsinger. Simulation based wing design for kite power. In U Ahrens, M Diehl, and R Schmehl, editors, *Airborne Wind Energy*, pages 325–338. Springer-Verlag Berlin Heidelberg, 2013.
[17] M Zanon, S Gros, and M Diehl. Airborne wind energy based on dual airfoils. *IEEE Conference on Decision and Control*, pages 1–8, 2012.
[18] awebox. Modelling and optimal control of multiple-kite systems for airborne wind energy. `https://github.com/awebox/awebox`, 2019.
[19] J A E Andersson, J Gillis, G Horn, J B, Rawlings, and M Diehl. CasADi: a software framework for nonlinear optimization and optimal control. *Mathematical Programming Computation*, 2018.
[20] A Wächter. *An Interior Point Algorithm for Large-Scale Nonlinear Optimization with Applications in Process Engineering*. PhD thesis, Carnegie Mellon University, 2002.
[21] HSL. A collection of Fortran codes for large scale scientific computation. `http://www.hsl.rl.ac.uk`, 2011.
[22] W Munters, C Meneveau, and J Meyers. Turbulent Inflow Precursor Method with Time-Varying Direction for Large-Eddy Simulations and Applications to Wind Farms. *Boundary-Layer Meteorology*, 159(2):305–328, 2016.
[23] J Mann. Wind field simulation. *Probabilistic Engineering Mechanics*, 13(4):269–282, 1998.
[24] L Gilling. Tugen - synthetic turbulence generator manual and user's guide. Technical report, Aalborg University. Aalborg, 2009.
[25] R C Storey, S E Norris, and J E Cater. An actuator sector method for efficient transient wind turbine simulation. *Wind Energy*, 18(4):699–711, 2015.
[26] N Troldborg, F Zahle, P-E Réthoré, and N N Sørensen. Comparison of wind turbine wake properties in nonsheared inflow predicted by different computational fluid dynamics rotor models. *Wind Energy*, 18(7):1239–1250, 2015.
[27] N Jenkins, A Burton, D Sharpe, and E Bossanyi. *Wind Energy Handbook*. Wiley, 2001.